Towards optical detection of a single electron

Moradi, A.

2

Matrix-induced linear Stark effect of single Dibenzoterrylene molecules in 2,3-Dibromonaphthalene crystal[1]

Absorption and fluorescence from single molecules can be tuned by applying an external electric field – a phenomenon known as the Stark effect. A linear Stark effect is associated to a lack of centrosymmetry of the guest in the host matrix. Centrosymmetric guests can display a linear Stark effect in disordered matrices, but the response of individual guest molecules is often relatively weak and non-uniform, with a broad distribution of the Stark coefficients. Here we introduce a novel single-molecule host-guest system, dibenzoterrylene (DBT) in 2,3-dibromonaphthalene (DBN) crystal. Fluorescent DBT molecules show excellent spectral stability with a large linear Stark effect, of the order of $1.5\,GHz/kVcm^{-1}$, corresponding to an electric dipole moment change of around 2 D. Remarkably, when the electric field is aligned with the a crystal axis, nearly all DBT molecules show either positive or negative Stark shifts with similar absolute values. These results are consistent with quantum chemistry calculations. Those indicate that DBT substitutes three DBN molecules along the a-axis, giving rise to eight equivalent embedding sites, related by the three glide planes of the orthorhombic crystal. The static dipole moment of DBT molecules is created by host-induced breaking of the inversion symmetry. This new host–guest system is promising for applications that require a high sensitivity of fluorescent emitters to electric fields, for example to probe weak electric fields.

1-This Chapter has been published in Chemphyschem 2019 Jan 7;20(1):55-61.

2.1. Introduction

Fluorescent polycyclic aromatic hydrocarbons (PAHs) are recently receiving increasing attention as bright and photostable single-photon emitters that can be integrated into on-chip quantum electronic devices.[1–4] Single-molecule fluorescence spectroscopy of PAHs at cryogenic temperatures has been used as a highly sensitive technique to optically probe the interactions of individual emitters with their local environments.[5–7] The spectral position of the narrow optical transitions (typical linewidth $30-50\,MHz$) is very sensitive to external perturbations, for example from electric fields. The shift in the spectral transition frequency between the ground and the excited state of a molecule in an electric field is commonly known as the Stark effect. Typically, the frequency shift has both linear and quadratic Stark contributions which depend on the change in electric dipole moment and in polarizability tensor, respectively, between the excited and ground states. [8,9]

Several host-guest systems with different contributions of the linear and quadratic Stark effects have been reported in the literature. [10–15] These studies mostly concentrated on centrosymmetric fluorescent emitters that should exhibit a quadratic Stark effect only. However, the central symmetry of the guest molecules is often broken in disordered host matrices, such as polymers, making it possible to observe the linear Stark effect. [9]

For terrylene in p-terphenyl, flipping of a host phenyl ring close to the guest leads to switching from a centrosymmetric to a non-centrosymmetric insertion, with distinct quadratic and linear dependences. [11,16] Nevertheless, a broad distribution of the linear Stark coefficients (often centered around zero) and low linear Stark coefficients for the majority of emitters still remain serious experimental limitations. For applications where the transition frequency should be tuned by an applied electric field, it is highly desirable to have a large fraction of single emitters responding uniformly (i.e. with similar Stark shifts) to the applied electric field. Furthermore, as the quadratic Stark effect is very weak in nature, the large linear Stark effect is advantageous. Such probes would enable faster and more reproducible tuning of single-photon emission, as well as a higher sensitivity of single molecules to small perturbations by local electric fields, including the optical detection of single electrons. [17–19]

Many of the probe molecules in single-molecule spectroscopy, such as dibenzoterrylene (DBT), [20] are centrosymmetric, which means that they do not intrinsically possess a permanent electric dipole moment. DBT has been recently a popular choice for fluorescent studies due to its excellent photophysical properties, including high brightness, photostability, single- emitter coupling to waveguides and to on-chip cavities, [21–23] and single-photon emission. [24]

A tunable single-molecule emission of DBT in the electric field can further facilitate quantum manipulation and integration of this molecule into molecular electronic quantum devices. Because they are easily synthesized, chemically identical and reproducible, single-molecule-based quantum emitters offer an appealing alternative to more frequently used single- photon sources, such as color centers in diamond, quantum dots, and other solid-state systems. [25–27] However, the well- studied and the most used molecular-based system, DBT in anthracene,

mainly exhibits quadratic Stark effect with very small linear coefficients (due to crystal defects) that are distributed around zero. [28] One strategy to induce a permanent electric dipole of the guest molecule is by the chemical synthesis of an asymmetric dye molecule. [29] Another strategy is to insert the symmetric guest molecule into a crystal built from asymmetric host molecules. This latter strategy is not risk-free, as the insertion of the guest into the host molecular crystal should not induce further defects nor any significant spectral diffusion. [30] The resulting doped crystals ideally should preserve the desirable spectral properties of the low-temperature fluorescent probe, such as narrow optical transitions, high spectral stability, and low spectral diffusion. Recent experimental and quantum chemistry studies on terrylene in di-substituted naphthalenes, such as 2,3-dichloronaphthalene and 2,3-dibromonaphthalene (DBN for short), have shown that these dihalogenated compounds can be suitable hosts for fluorescent PAH molecules. [31,32] Here we show that the electro-negativity of halogen atoms, combined with the herring-bone crystalline structure of the host, is able to induce large electric dipoles on a centrosymmetric molecule such as dibenzoterry-lene. We introduce a novel host-guest system based on DBT in DBN and report for the first time on a large linear Stark shift homogeneously affecting all fluorescent molecules by matrix-induced symmetry breaking.

2.2. Experimental section

2.2.1. Crystal growth

DBN used in this work was purchased from Ark Pharm Inc. High- quality single crystals of zone-refined DBN doped with DBT molecules were obtained by co-sublimation at $\sim 0.2\ (bar)$ of argon gas. To prevent perturbations from the convection flow in the sublimation chamber, the sublimator was kept horizontal during growth. The sublimation-grown crystals develop along the $(a.b)$ plane as thin mm-sized plates or flakes, with a typical thickness of few microns along the c-axis.

2.2.2. Optical microscopy

A well-defined single crystal free of visible defects was carefully transferred to a silica substrate on which interdigitated gold electrodes had been deposited by lithography (see Figure 2.1.b). The electrodes were $200\ nm$ thick and were separated by a distance of $10\ \mu m$. The external electric field was varied through the voltage applied to the electrodes. The crystals were placed on the chip at the desired angle between the electric field and the crystallographic a-axis, determined by separately measuring the orientation of the transition dipole moment of DBT impurities. To this aim, the crystal was placed on a rotating stage and excited at normal incidence by a $756\ nm$ laser beam with linear polarization in the $(a.b)$-plane of the crystal. Fluorescence images were recorded with a sensitive CMOS camera (Hamamatsu, Orca Flash 4.0) while rotating the stage.

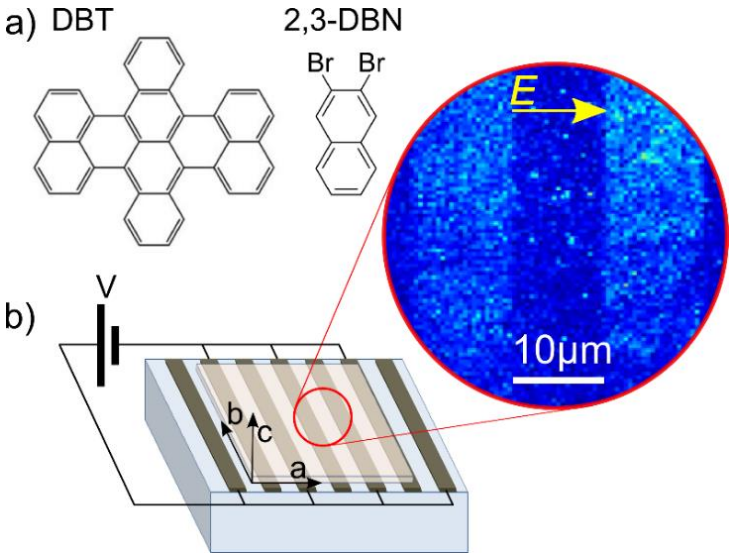

Figure 2.1. a) Molecular structures of DBT and 2,3-DBrN. b) Schematic of the chip for Stark effect measurements with a crystal placed on the top of electrodes. The axes designate the crystallographic orientation of the crystal in the plane of electrodes. Zoom-in shows a confocal fluorescence microscopy image of the crystal containing fluorescent DBT molecules. The electrodes are visible through stronger light scattering.

All single-molecule measurements were done at 1.2 K in a home-built liquid-helium bath cryostat. Single DBT molecules were excited by a tunable continuous wave Ti:Sapphire laser (Coherent,899–21) with a $2\,MHz$ bandwidth. The sample was scanned in a confocal arrangement using a scanning mirror (Newport, FSM-300-01). The fluorescence light was collected by a cryogenic objective (Microthek, $NA = 0.8$) and detected by a single-photon counting module (Excelitas Single Photon Counting Module, SPCM-AQRH-16) with a set of filters (Chroma HQ760LP and Semrock FF02-809/81) in the detection path.

Bulk fluorescence excitation and emission spectra were obtained at 5K using a Ti:Sapphire laser (Coherent, Mira-HP). For the detection path, a scanning monochromator (McPherson, 207) and a photo- multiplier (EMI, 9659) operating in photon-counting mode were used. The fluorescence excitation spectrum was obtained by scanning the laser while the monochromator was set to $773.6\,nm$ (a band pass filter Chroma D780/20 was used in the detection path). For the fluorescence emission spectrum, the laser was in resonance with the vibronic component located at $740.3\,nm$ (with Semrock FF01-785/62 filter in the detection path).

2.2.3. Quantum chemistry calculations

All calculations in this work were done with the Gaussian 09 package. [33] Like in our previous works [32,34] optimization of the geometry of DBT placed inside the rigid crystalline lattice was done with the aid of the ONIOM(B3LYP/6-31G(d,p):UFF) procedure, where B3LYP/6-31G(d,p) is used for the DBT molecule (as so-called high layer in the division of the calculated system) and UFF method for the DBN lattice (low layer). In our calculations we consider a crystal composed by $3 \times 2 \times 2$ unit cells (i.e. 96 molecules of DBN) with geometry based on the orthorhombic P_{bca} unit cell of DBN crystal, as described in previously published

crystallographic data. [32,35] A DBT molecule replaces three molecules of DBN aligned along the crystal a-axis. Calculations were strongly limited by the requirements of the computational memory and time, especially for the electronically excited states. Therefore, the simplest TD B3LYP/STO-3G method was used for calculations of the dipole moments of both, the whole system and the individual components.

2.3. Results

2.3.1. Photophysical properties of the system

The molecular structures of DBT and DBN are shown in Figure 2.1.a. A platelet-like crystal of DBT/DBN was optically contacted to a custom-made glass chip with electrodes (Figure 2.1.b). First, we studied the bulk photophysical properties of the DBT/DBN system. Figure 2.1.a displays the bulk fluorescence excitation (blue curve) and emission (red curve) spectra of DBT/DBN. A single, inhomogeneously broadened line at about $756.6\ nm$ is found at the same wavelength in the excitation and fluorescence spectra. Thus, it indicates a purely electronic zero-phonon line (ZPL) of this system, and it was the only one we could find. The inhomogeneous linewidth of the ZPL is $\sim 5\ cm^{-1}$. The absence of other resonant absorption and fluorescence peaks points towards a *single spectroscopic site* in this host-guest system.

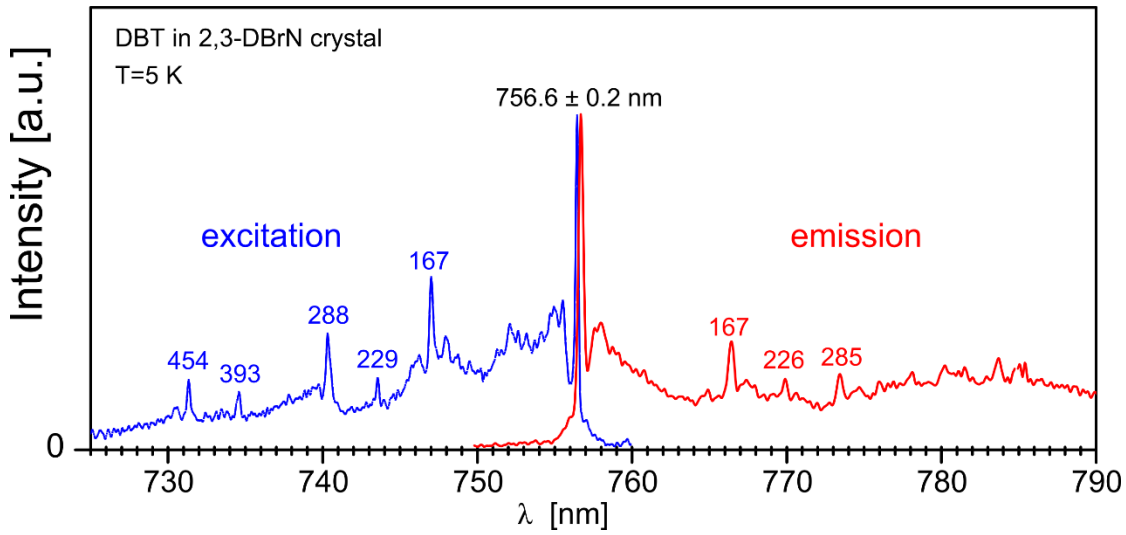

Figure 2.2. Fluorescence excitation spectrum (blue) with fluorescence detection at wavelengths longer than $773.6\ nm$, and fluorescence spectrum (red) excited at $740.3\ nm$. The number above each vibronic line indicates the vibration frequency (shift from the ZPL) in reciprocal centimeters (cm^{-1}).

For the cryogenic single-molecule experiments, the laser was tuned at $756.4\ nm$ to excite individual DBT molecules from the ground vibronic level of the ground state ($|g.v=0\rangle$) to the ground vibronic level of the excited electronic state ($|e.v=0\rangle$). In the following, we will use the static dipole moment vectors μ_g and μ_e in the ground and excited state, respectively, as well as their difference $\Delta\mu = \mu_e - \mu_g$. The transition matrix element between these two states is another vector, noted μ_{eg}. The studied system also provided a conveniently large number of single emitters within a $3GHz$ single frequency scan.

Figure 2.3.a shows the excitation spectra of more than 20 DBT molecules recorded over $250\,s$ of repetitive frequency scans. Each horizontal line indicates an individual DBT molecule within the focal spot of the laser beam, showing excellent spectral stability in time. No significant frequency jumps or spectral diffusion have been observed, even during longer measurements. Similarly, we did not observe significant broadening of the homogeneous linewidth, as shown for a single molecule in Figure 2.3.b. The full width at half-maximum (FWHM) was extrapolated from the measured saturation curves of 30 molecules (Figure 2.3.c). The average FWHM of $37 \pm 4\,MHz$ agrees well with the observed fluorescence lifetime of DBT in DBN, $4.84\,ns$ (see Figure S2.1 in the Supporting Information). The number of detected counts at saturation was around 80,000 cps for most molecules, a typical detection rate for well-oriented DBT molecules.[20] These measurements already indicate very favorable photophysical properties of the DBT/DBN system for single-molecule spectroscopy.

We point out here that the size of the host halogen atoms most likely also plays a role in stabilizing the system. We performed similar experiments with 2,3-dichloronaph-thalene as host, but DBT molecules in this system turned out to be significantly less photostable. The introduction of halogen atoms to the aromatic host could be a common strategy to induce a linear Stark shift. TÜrschmann et al. have reported linear Stark effect on DBT in *para-dichlorobenzene*, although the authors noted that different individual DBT molecules in this system respond differently to the electric field. [36]

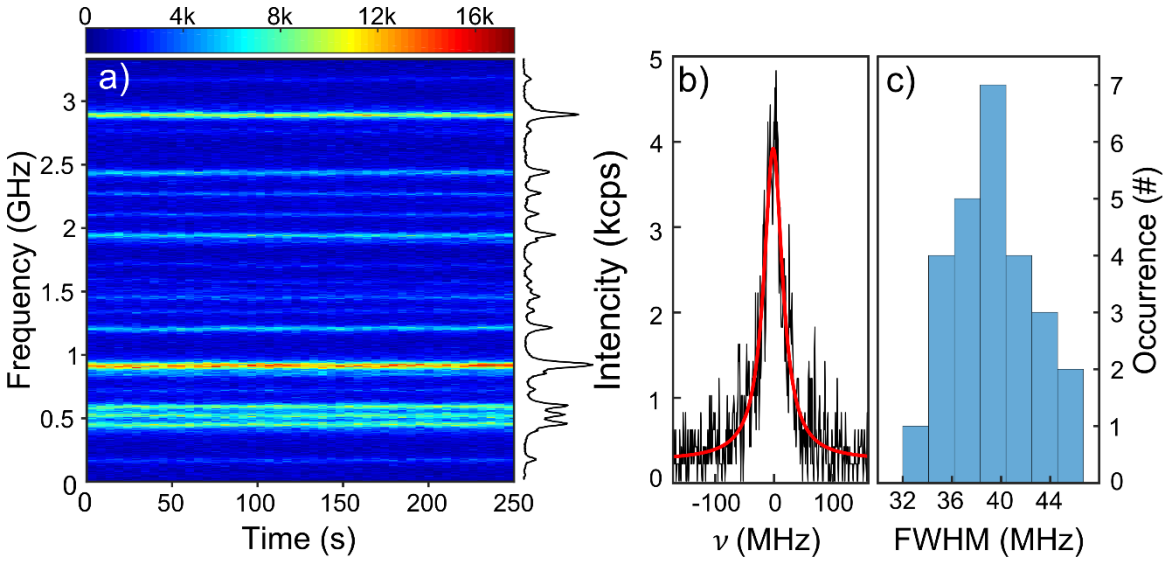

Figure 2.3. a) Time traces of more than 20 single molecules measured at 756.4 *nm*. The color scale units are counts per second. b) Single DBT molecule ZPL spectrum fitted with the Lorentzian profile. c) Histogram of the single-molecule homogeneous linewidth.

2.3.2. Stark effect experiments

The Stark shift of single-molecule ZPLs was measured by applying a variable voltage on the electrodes. In all Stark measurements the applied electric field varied from $-1kV/cm$ to $1kV/cm$ while the laser was scanned for each voltage applied. The uniformity of the electric field was ensured by measuring molecules at the distance of $5 \pm 1\,\mu m$ from the

edges of the electrodes and within the same focal plane as the electrodes (Figure 2.1.b). Figure 2.4.a presents the Stark shift of more than 20 DBT molecules when the a-axis of the crystal was aligned along the applied electric field. The large linear Stark shifts in the order of 1.5 $GHz/kVcm^{-1}$ proved that the strategy of inducing static dipole moments in the guest molecules by the use of asymmetric host molecules is effective. Remarkably, all molecules within the scanned confocal volume exhibited similar absolute values of the Stark coefficients, as shown in Figure 2.4.b. We find two distinct sub-populations of molecules, but with identical absolute values of their Stark shift (1.4 $GHz/kVcm^{-1}$).

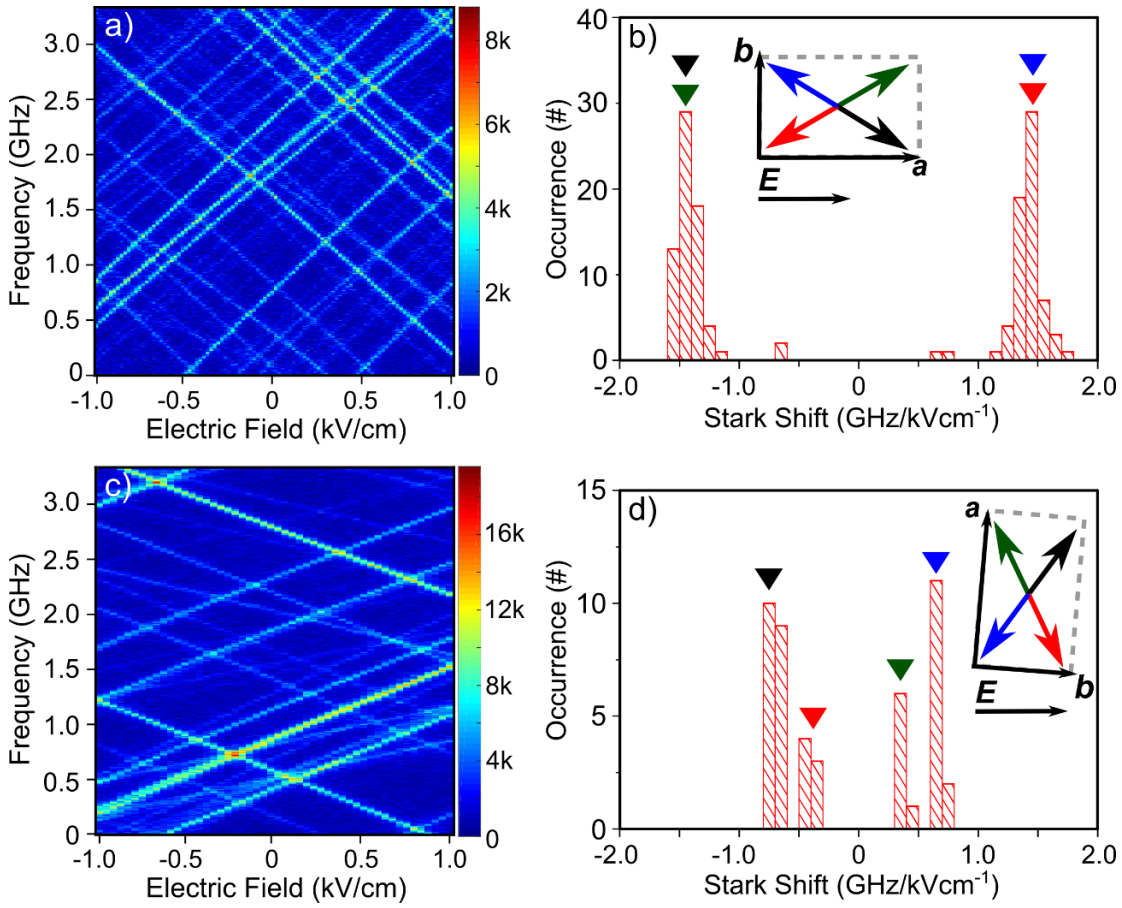

Figure 2.4. Stark shifts of DBT single molecules in an electric field nearly parallel or perpendicular to the a-axis. a) Electric field nearly parallel ($2 \pm 5°$) to the a-axis, and b) corresponding histogram of the Stark shift. c) Electric field nearly perpendicular ($85 \pm 5°$) to the a-axis, and d) corresponding histogram of the Stark shift. The color scales in (a) and (c) are in counts per second. Insets in (b) and (d) indicate the orientation of the crystal (and 4 molecular dipoles) in the (a,b) plane with respect to the electric field, E. The color-coded triangles indicate the values of the Stark shifts for the corresponding four dipoles.

The opposite slopes of the two sub-populations indicate that the electric dipole difference vector, $\Delta\mu$, can have either a positive or a negative projection onto the applied electric field, directed along the a-axis. Previously, large linear Stark shifts of similar magnitudes were observed on single molecules of terrylene in amorphous polyethylene (up to 2 $GHz/kVcm^{-1}$). [9] In crystalline hydrocarbon matrices, such as naphthalene, p-terphenyl and n-hexadecane, the Stark shifts of terrylene and dibenzathranthrene are comparatively weak, with the highest recorded linear coefficients in the order of 200 $MHz/kVcm^{-1}$. [10,11,13] In

stark contrast to these previous studies, almost all molecules in our system exhibit equally large linear Stark shifts, without any non-responsive molecules. Such a large and homogenous response of all emitters to an external electric field has never been reported previously.

Further inspection of the crystal orientation in the electric field shows that the magnitudes of the Stark shift depend on the exact alignment of the crystal in the electric field. As expected, the minimum in the Stark response is reached when the crystallographic a-axis is nearly perpendicular to the electric field (Figure 2.4.c). For an arbitrary orientation of the crystal with respect to the electrodes, we found four distinct sub-populations of molecules with different Stark shifts, and two-by-two opposite values. For example, for an angle $\varphi \sim 85°$ between the electric field and the a-axis, we find Stark shifts centered around ± 0.4 and $\pm 0.7\ GHz/\ kVcm^{-1}$, as shown in Figure 2.4.d. This result suggests at least 4 distinct dipole orientations in the electric field, related to each other by the symmetry on the crystal. Interestingly, the maximum value of the Stark coefficient ($1.56\ GHz/kVcm^{-1}$) is reached for a crystal with an angle φ of $20°$ between the a-axis and the electric field (Figure S2.3). The measured Stark coefficient maximum translates into the electric dipole moment change of 2.1 D, if a local-field correction factor of 1.5 is applied.

We can now consider our results as a special case of four dipoles in an electric field E situated in the (a, b) plane, which is our experimental arrangement. The linear Stark shift is proportional to a scalar product of $\Delta\mu$ and E, i.e. $h\Delta\nu = -\Delta\mu \cdot E$. Here we consider the effective electric field which includes the local-field correction. As discussed later, the symmetries of the host crystal give rise to four possible projections of the dipole moment onto the field, which can be expressed using the angle φ between the electric field and the crystal's a-axis, as well as the angle θ between the a-axis and the $\Delta\mu$ a particular molecule taken as a reference (see Figure 2.5). Note that θ is an intrinsic property of the crystal, whereas we can give f arbitrary values by orienting the crystal with respect to the electrodes. By using the two angles θ and φ, the Stark shift will be different for each of the four *differently oriented* guest dipoles. The Stark shift of the reference molecule will then be $h\nu = -\Delta\mu_{max} \cdot E\cos(\varphi + \theta)$ or expressed as the frequency change, $\Delta\nu = -\Delta\nu_{max}\cos(\varphi + \theta)$. For the three other molecules deduced by mirror symmetries on glide planes (a,c) and (b,c), the shifts are: $\Delta V = \Delta V_{max}\cos(\varphi - \theta)$, $\Delta V = -\Delta V_{max}\cos(\varphi + \theta)$, $\Delta V = -\Delta V_{max}\cos(\varphi - \theta)$ corresponding to four possible orientations of the dipole moments in the (a,b) plane.

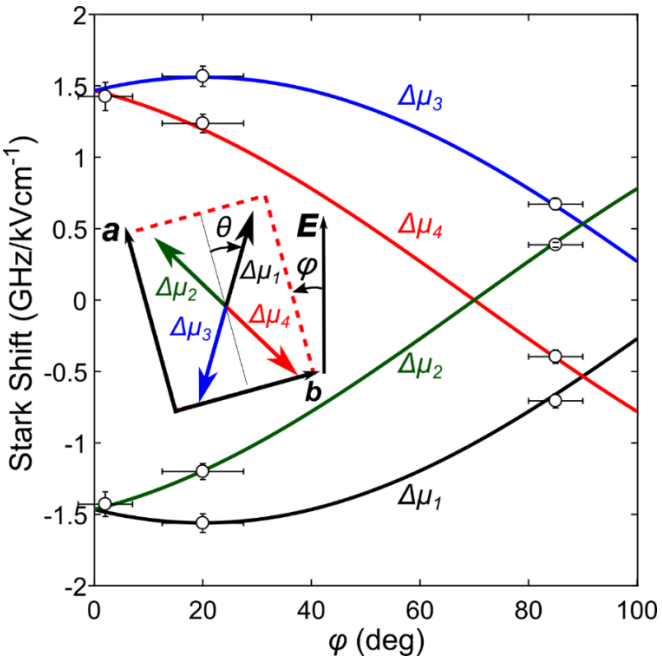

Figure 2.5: Angle-dependent Stark shift as a function of the angle, φ, between the a crystallographic axis and the electric field. The Stark shift is calculated for four electric dipoles (rotated $-\theta+\varphi, \theta+\varphi, \pi-\theta+\varphi, \pi+\theta+\varphi$ and compared to the experimental data (hollow circles). The simulated values are determined for the maximum of the Stark shift $1.56 \pm 0.06\ GHz/kVcm^{-1}$ and $\theta = 20°$. The inset illustrates the orientation of the four dipoles used in calculation; a and b axes, electric field vector E, as well as angles θ and φ are shown.

Figure 2.5 shows the dependence of the Stark shift on the tilt angle φ of the crystal's a-axis with respect to the electric field. The calculated Stark shift as a function of φ (solid lines) coincided with the experimental data (circles) for $\theta = 20 \pm 5°$. Other values of θ could not match our results, as shown in Figure S2.4. The results also show that the four values of the Stark shift should merge into two values when the crystal is perfectly aligned with the electric field ($\varphi = 0°$), which is the case for the measurement shown in Figure 2.4.a. The maximum of the Stark shift will be, however, recorded for the alignment angle $\varphi = -\theta$, when E coincides with one of the four projections of $\Delta\mu$ vectors. These experimental findings will be generalized for an arbitrary electric field in the Discussion section.

2.3.3. Quantum chemistry calculations

To understand the origin of the large Stark shift of DBT, we have performed quantum chemistry calculations looking for the structure of a DBT molecule and its dipole moments, which may be affected by interaction with the surrounding DBN host molecules. In the calculations, a guest DBT molecule was embedded in a P_{bca} orthorhombic unit cell of DBN (Figure S2.5) by replacing 3 host molecules along the crystal a-axis and was surrounded by 96 DBN molecules (12 elementary cells). The result of ONIOM (B3LYP/6-31G (d, p): UFF) optimization is shown in Figure 2.6.a (for coordinates of the optimized DBT see Tab. S2.1). It is visible that the embedded DBT molecule loses the C_{2h} symmetry characterizing the isolated DBT. [37]

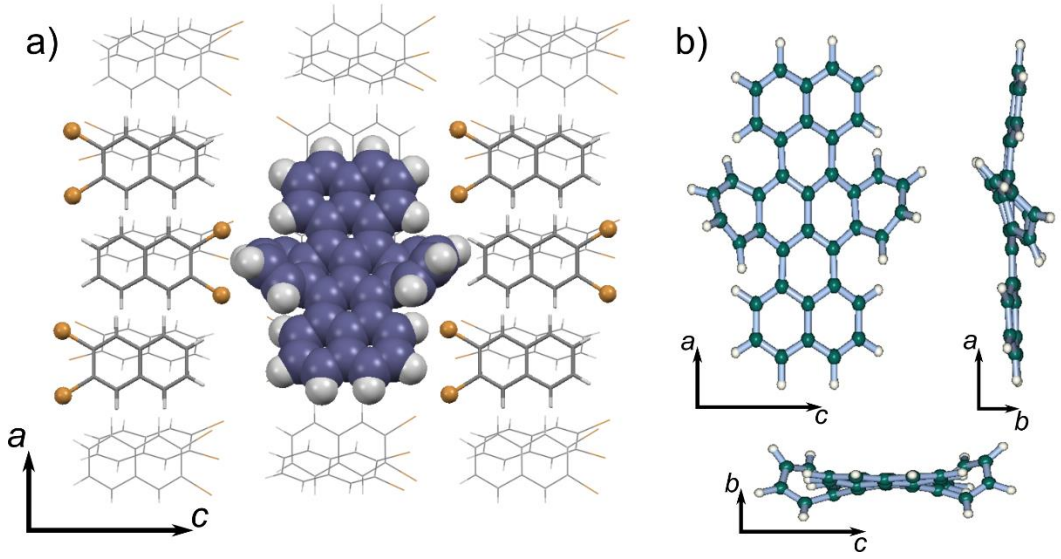

Figure 2.6: a) Insertion site, visualized in the (a,c) plane. The DBT molecule is represented in space-fill molecular model, replacing 3 host molecules; the adjacent DBN molecules (along a-axis) are highlighted as capped sticks. Bromine atoms (golden balls) are highlighted for convenience. b) Host-induced distortion and bending of the guest DBT molecule visualized in all three planes. For more detailed crystallographic information about the unit cell of the host matrix, see Figure S2.5.

Figure 2.6.b illustrates the resulting large distortion of the terrylene core and the tetracene unit of DBT. Structural changes of the DBT molecule are accompanied by changes of the static dipole moments in the ground and excited states. A free-space DBT molecule does not possess any permanent dipole moment. The total dipole moment of each unit cell of the DBN crystal (containing 8 DBN molecules) is also zero, although each of the DBN molecules has a non-zero dipole moment (1.48 D). Creating an empty cavity in the DBN crystal by removing three DBN molecules along the axis a results in the appearance of a dipole moment of 1.8 D, directed mainly along the a crystal axis (see Table S2.3). The asymmetric distribution of the electron density at the DBT molecule (with the DBN crystal optimized structure) has relatively large components of the electric dipole moment along the two crystal axes (a and c), as shown in Table S2.2. The total dipole moment of the whole system, i.e. DBT in DBN crystal, after optimization of DBT structure is 2.46 D (Table S2.3). The difference between dipole moment vectors of the crystal with the empty cavity and with the cavity filled with DBT is 1.53 D. This value is greater than the dipole moment calculated for the isolated DBT molecule in its crystal-deformed geometry, 0.69 D (Table S2.2). Thus, the interaction of DBT (in the electronic ground state) with the surrounding DBN molecules leads to a significant increase of the dipole moment of the whole system.

The isolated DBT molecule in the distorted geometry optimized in the DBN crystal also possesses a nonzero permanent dipole moment in the excited singlet S1 state, equal 0.38 D according to our calculations (Table S2.2). The calculated difference between dipole moments in excited S_1 and ground S_0 electronic states is $|\Delta\mu| = 0.47D$. The transition moment μ_{eg} reaches 7.8 D and is oriented almost perfectly along the molecule's long axis (Table S2.2), as found experimentally. An interesting observation is that the vector

difference $\Delta\mu$ responsible for the large Stark effect, is directed mainly along the transition dipole moment μ_{eg} (and thus along the a-axis of the host crystal).

Table 1. Components along the crystal axes of the transition dipole moment μ_{eg} and dipole moments μ_g, μ_e, $\Delta\mu = \mu_e - \mu_g$ of DBT obtained for the simulation cell with 28 host molecules (see Table S2.4 for details). All values are in D (where $1D = 3.34 \cdot 10^{-30} Cm$); a-, b-, and c-axis, represent the projections of the calculated vectors on the crystallographic axes of the crystal, whereas $|\mu|$ represents the modulus of the corresponding vector.

	a-axis	b-axis	c-axis	$\lvert\mu\rvert$
μ_{eg}	8.0150	0.3820	0.4592	8.0372
μ_g	−0.6149	−0.6587	−7.7383	7.7906
μ_e	0.1438	−0.7913	−8.4195	8.4579
$\mu_e - \mu_g$	0.7587	−0.1326	−0.6812	1.0282

Unfortunately, the size of the system required to calculate the dipole moment in the electronic excited S_1 state must be much smaller than for the ground S_0 state. Therefore, the s_1 calculations were performed for a limited number of 28 surrounding host molecules, with the DBT geometry optimized in the ground state. Summarizing these results in Table 1 we may conclude that the dipole moment in the excited S_1 state increased by about 1 D, which is larger than the value calculated for the isolated DBT in the optimized geometry Similar results were obtained with smaller simulation cells (Supporting Information Table S2.4). The projection of $\Delta\mu$ onto the crystal a-axis is found to be 0.76 D, with an angle of 10° between the a-axis and $\Delta\mu$ see Table 1). This value matches reasonably well with $\theta = 20°$ derived from the experiment.

2.4. Discussion

Before discussing possible DBT insertions in the DBN crystal, let us briefly recall the structure of this crystal. DBN crystallizes in the orthorhombic P_{bca} system, which is characterized by three glide planes, with glide mirrors (a,b), (b,c), (c,a), and a center of symmetry at the center of the unit cell. The unit cell contains 8 molecules arranged in a herring-bone pattern. These molecules are all related by mirror symmetries in the glide planes, as illustrated in Figure S2.5. The 8 molecules in the unit cell thus cover all the 8 possible images of any particular molecule in the 3 glide planes (i.e., after suitable translations, see Figure S2.5), in the 3 screw axis rotations, which are products of two glide mirror symmetries, and in the inversion. Embedding a DBT molecule in this crystal requires removing 3 host molecules. Quantum chemistry calculations indicate that the most favorable way to do this is to replace 3 DBN molecules along the crystallographic a-axis (Figure 2.6.a). Indeed, this is in accordance with the experimental finding that the DBT transition dipole moment, directed along the long DBT axis, is roughly aligned along the a-axis of the

crystal. Taking the crystal structure into account, we find that the substitution can be realized in 8 different manners, taking each molecule in the DBN unit cell as the starting point for the substitution of 3 DBN molecules along the a-axis. Moreover, these 8 distinct insertion sites are all related by the same mirror symmetries in the glide planes as the original host molecules. Therefore, they are completely equivalent from a spectroscopic point of view, which nicely explains why only one single spectroscopic site is observed (Figure 2.2).

Let us now consider any vector V (components $V_a.V_b.V_c$ in the crystal's orthonormalized reference frame) related to a molecule (1) in the DBN unit cell (see Figure S.5). The associated vectors for each of the seven other molecules will be deduced from V through mirror symmetries and their products, leading to 8 vectors with components $\pm V_a.\pm V_b.\pm V\_c$. In particular, the Stark effect is determined by the dipole moment change $\Delta\mu$ of molecule (1). The symmetry of the crystal thus gives rises to 8 possible dipole moment changes, $\Delta\mu_i(\pm\Delta\mu_a.\pm\Delta\mu_b.\pm\Delta\mu_c)$. To each possible DBT insertion site we can thus associate one of these 8 $\Delta\mu_i$ vectors. Note, however, that these 8 vectors all have equal magnitudes of $|\Delta\mu|$. Upon application of an external electric field E with components $(E_a.E_b.E_c)$, we obtain 8 possible linear Stark effects with the shifts: $h\Delta\nu = (\pm\Delta\mu_a E_a \pm \Delta\mu_b E_b \pm \Delta\mu_c E_c)$, i. e., 8 sub-populations of molecules with different Stark shifts. In the special case of a field situated in one of the planes, e. g. (a, b), $E_c = 0$ and we find only four sub-populations, $h\Delta\nu = -(\pm\Delta\mu_a E_a \pm \Delta\mu_b E_b)$. Similarly, for a field oriented along one of the crystal axes, e. g. the a-axis, we find only two sub-populations with shifts $h\Delta\nu = \mp\Delta\mu_a$. The cases of two and four distinct sub-populations are observed experimentally (see Figure 2.4). Finally, we note that, according to calculations, $\Delta\mu$ can have a significant component along the c axis, but the effective electric field component E_c should be negligible in our experiment. A small angle between the crystal and the chip surface (1– 5°), or a small displacement of the molecule with respect to the electrode plane, can account for the deviations in the order of $50–100\ MHz/kVcm^{-1}$. Because of the inhomogeneous broadening, these values are too small to be unambiguously determined experimentally.

2.5. Conclusions

We presented a new host-guest system for single-molecule fluorescence spectroscopy based on DBT in 2,3-dibromonaphthalene (DBN). The system is the first successful demonstration of a strategy to use an asymmetric and polar host matrix to induce large static dipole moments in otherwise centrosymmetric guest molecules. This strategy leads to a large linear Stark effect in the order of $1.5\ GHz/kVcm^{-1}$ for DBT in DBN. DBT molecules in the system behave remarkably well–they all respond similarly to the applied electric field, showing at the same time excellent spectral stability and narrow single-molecule resonances of about $40MHz$ width. Our results were further complemented by quantum chemistry calculations, which indicated host-induced symmetry breaking in DBT molecules. By considering the symmetry of the host crystal, we have explained why embedding of DBT in DBN crystal, while exhibiting a single spectroscopic site, can lead to up to 8 different Stark coefficients in an applied electric field with arbitrary orientation. This system is an excellent candidate for single-molecule spectroscopy of DBT– an increasingly popular single-photon

emitter. In addition, the large and homogeneous linear Stark response of the probe could be used for sensing local electric fields and for a precise tuning of the single-molecule emission wavelength over a large spectral range.

2.6. Supporting information

compare to the extrapolated linewidth of single molecules at low temperature and low power, we measured ensemble fluorescence decays of DBT in DBN crystals at 5 K, using a confocal fluorescence microscope. The extracted lifetime, 4.84 ns, corresponds to a life-time limited linewidth of 33 MHz, in good agreement with the measurements (36-40 MHz, see Figure 2.3.c).

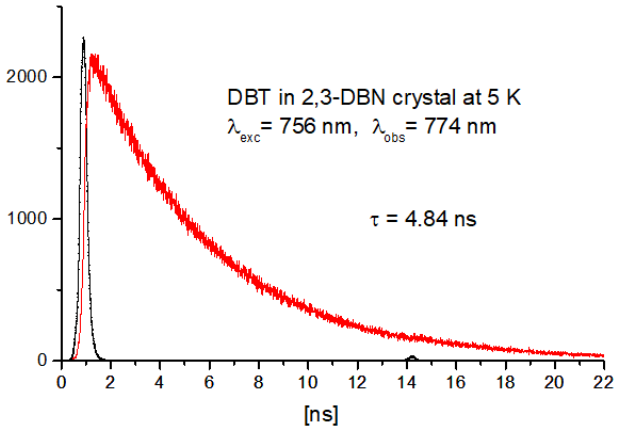

Figure S2.1: Fluorescence lifetime decay measurement of DBT in 2,3-DBN (red line), as measured for an ensemble at 5 K using a confocal fluorescence microscope. The instrument response function is shown in black. The fluorescence emission of DBT was excited at 756 nm and detected using a long-pass filter at 774 nm and an SPCM-AQR-14 photon counting module.

2.6.1. Crystal Alignment for the Stark Experiment

A DBT/DBN single crystal was aligned to the custom-made electrodes and optically contacted to them, as described in the experimental section. We aligned the crystal based on the guest transition dipole moment. As a verification, we could check that the cleavage planes of the crystal ((a, c) and (b, c) planes) appear as cracks due to thermal stress after the cryogenic experiment (Figure S2.2). More cracks are observed along the direction. This is expected based on the crystal packing presented in Figure 2.6.

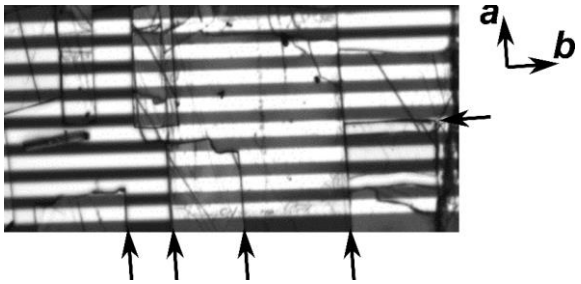

Figure S2.2: Optical micrograph of a cracked crystal taken after a cryogenic experiment. The bright parallel bands are the gold electrodes, with the interspacing distance of 10 µm. The direction of several of the cracks reveals cleavage planes of the crystal along the a-axis, here parallel to the applied electric field, i.e., perpendicular to the electrodes.

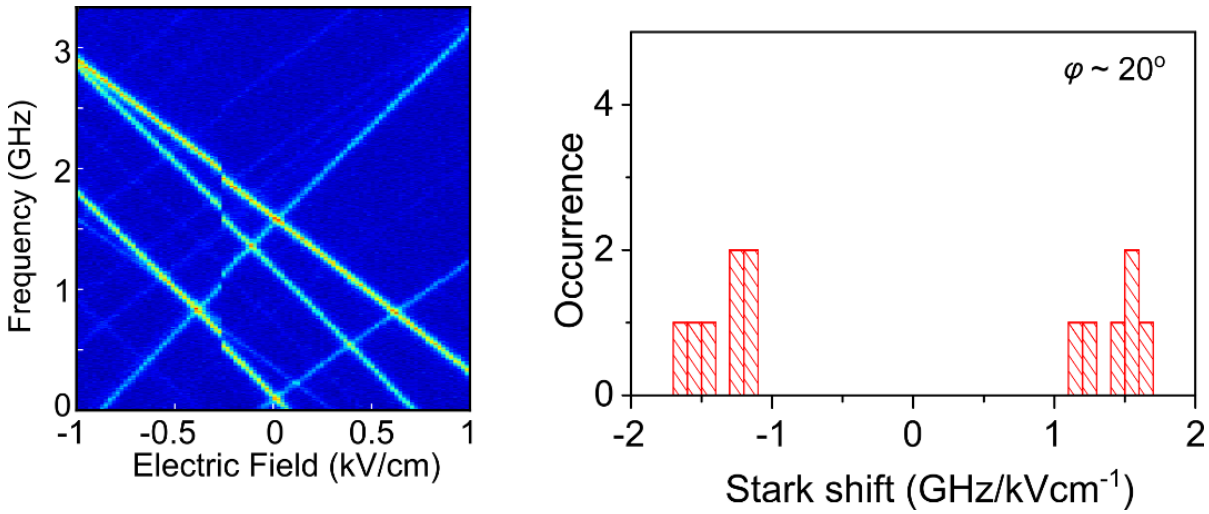

Figure S2.3: Left: The highest value of the Stark shift (1.56 GHz/kVcm^{-1}) is observed for the angle φ = 20° between the electric field and the crystal a-axis. Right: Corresponding histogram of the Stark shifts clearly showing four sub-populations. The discontinuity observed for electric field ~ - 0.3 kV/cm is due to a jump in the electric voltage source.

2.6.2. Calculation of the Stark Shifts: Four-dipoles Model

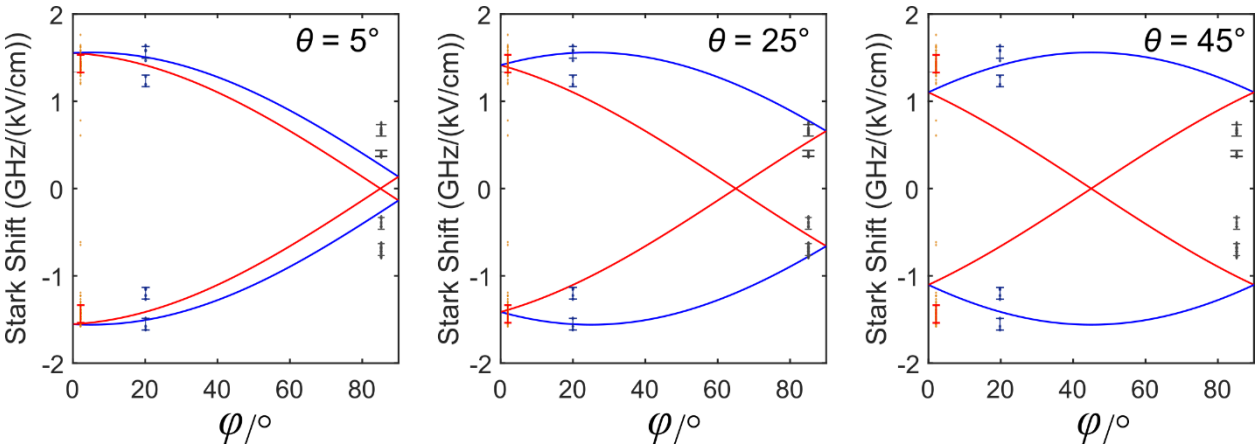

Figure S2.4: Calculated Stark shifts (red and blue lines) for three different values of θ (angle between the a-axis and the dipole moment difference vector **Δμ**. The angle φ is the angle between the a-axis and the electric field, as described in the main text. Experimental data points are shown as dots with error bars and compared with calculations (solid lines) for 3 values of θ.

Although up to eight populations of molecules with different Stark effects can be expected in the general case, we could fit our data with four sub-populations only because the electric field was applied in the (a,b) plane of the crystal. For the simple model explained in the main text, we obtain a sinusoidal variation of the Stark coefficient with the angle φ between the crystal a-axis and the electric field. Depending on the angle θ between the dipole moment difference of one population with the a-axis, we obtain four different dependences for the Stark shift as a function of φ. The plot of Figure S2.4 shows global fits of all measurement points for different values of θ. The value θ = 20° ± 5° gives an excellent agreement with the measurements.

2.6.3. Unit cell and glide planes of the DBN host crystal

2,3-dibromonaphthalene crystallizes in the orthorhombic P_{bca} space group with 8 molecules in the unit cell (Figure S2.5); the lattice constants are: a = 11.692 Å, b = 7.545 Å, c = 20.193 Å; see ref. 24 of the main text for more details. Each molecule in the unit cell is related to a reference one, for example molecule (1), by a symmetry operation, such as a glide plane. A glide plane is a symmetry operation associating (1) a reflection in the plane with (2) a translation parallel to that plane. The glide planes of 2,3-DBrN are shown as the red lines in Figure S2.5.

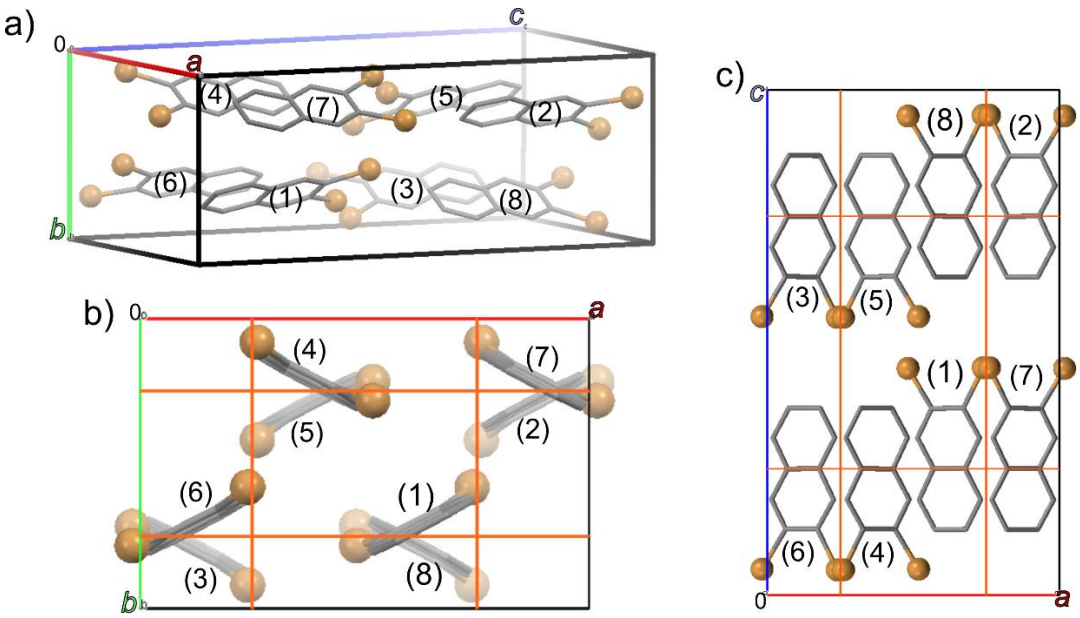

Figure S2.5: a) Unit cell of 2,3-dibromonaphthalene with numbered molecules. Molecule (1) is taken as a reference. b,c) Projections of the unit cell and corresponding glide planes (red lines), shown in (b) a-b, and (c) a-c plane. Each of the molecules in the unit cell is related to another one by glide planes or products thereof. Bromines are highlighted as golden balls to stress the broken symmetry of DBN molecules, whereas hydrogens are omitted for clarity.

The 7 operations relating a reference molecule (e.g., mol. (1)) to the others molecules in the cell are: i) the inversion in the unit cell center (with mol. (5)), ii)-iv) 3 glide planes, associating translations with reflections in (a,b) (mol. (6)), (b,c) (mol. (7)), and (c,a) (mol. (8)) planes, v)-vii) 3 screw axes (2-fold) associating translations with rotations around a (mol. (3)), b (mol. (4)), c (mol. (2)) axes. The screw axis rotations are products of 2 glide plane reflections, and the inversion is the product of the 3 of them. All molecules in the unit cell are thus related to one another by glide planes or products of glide planes.

The symmetry operations for the designated molecules, in respect to molecule (1), are:

Molecule #	Description	Symmetry Operation
(1)	Identity	$x.y.z$
(2)	Screw *c*-axis (2-fold)	$\frac{1}{2}-x.-y.1/2+z$
(3)	Screw *a*-axis (2-fold)	$\frac{1}{2}+x.\frac{1}{2}-y.-z$
(4)	Screw *b*-axis (2-fold)	$-x.\frac{1}{2}+y.1/2-z$
(5)	Inversion center	$-x.-y.-z$
(6)	Glide (*a*, *b*) plane	$\frac{1}{2}+x.y.1/2-z$
(7)	Glide (*b*, *c*) plane	$\frac{1}{2}-x.\frac{1}{2}+y.z$
(8)	Glide (*a*, *c*) plane	$x.\frac{1}{2}-y.1/2+z$

2.6.4. DFT Calculations

Table S2.1: Cartesian coordinates of DBT optimized in DBN crystal by ONIOM(B3LYP/6-31G(d,p):UFF) method. E(RB3LYP) = -1460.01164427 au; μ= 0.6954 D.

atom	***x***	***y***	***z***	***atom***	***x***	***y***	***z***
	5.813991	-1.244366	0.050208	C	-1.151752	-3.433592	-0.904995
C	5.132390	-0.004193	0.119411	C	-0.700916	-4.420353	-0.153958
C	5.112554	-2.402917	-0.205659	C	0.200473	-4.263671	0.947477
C	3.700885	0.013277	0.066504	C	1.139221	-3.340861	0.728851
C	3.712366	-2.378853	-0.316408	C	-1.227788	3.510411	-1.015905
C	2.987591	-1.204350	-0.082837	C	-0.894976	4.548123	-0.242088
C	5.830300	1.225021	0.174225	C	0.056581	4.319369	0.821454
C	2.980012	1.246581	0.056758	C	1.024911	3.413003	0.689233
C	1.533804	-1.146912	-0.095970	H	6.897952	-1.252687	0.125156
C	3.728360	2.420129	-0.011581	H	3.231368	3.365528	-0.167085
C	5.128485	2.402954	0.069944	H	5.656906	3.341109	0.012511
C	1.519874	1.214849	-0.050380	H	5.640065	-3.341666	-0.347541
C	0.793285	0.031293	-0.124301	H	6.915631	1.222116	0.224144
C	0.716992	2.335732	-0.143304	H	3.199691	-3.287317	-0.605484
C	-0.669035	0.037769	-0.130308	H	2.102236	-3.300159	1.171391
C	0.742275	-2.265634	-0.064930	H	0.345961	-5.025335	1.689127
C	-0.624369	-2.221621	-0.470110	H	-0.898886	-5.375432	-0.524632
C	-0.641094	2.291898	-0.627001	H	-1.889932	-3.545389	-1.677632
C	-1.408219	-1.140152	-0.244871	H	-2.051000	3.559127	-1.708697
C	-1.422463	1.192894	-0.343712	H	-1.426465	5.457366	-0.471352
C	-2.863662	-1.250468	-0.110214	H	0.167049	4.875715	1.731306
C	-2.896330	1.194626	-0.161058	H	1.838288	3.341627	1.398016
C	-3.597991	-0.043904	-0.065115	H	-3.106074	3.271182	0.160333
C	-3.549187	-2.448153	0.124286	H	-5.587616	3.227551	0.464997
C	-4.946274	-2.486730	0.263203	H	-6.806434	1.110008	0.374913
C	-5.680056	-1.325260	0.227138	H	-6.763261	-1.336239	0.305808
C	-5.016702	-0.080758	0.128470	H	-5.435433	-3.445403	0.408160
C	-5.726739	1.132081	0.257861	H	-3.010670	-3.373897	0.231376

Table S2.2: Structure of the DBT molecule as deformed in the crystal field (see Table S2.1). Components of the dipole moments in the electronic ground S_0 and excited S_1 states of a DBT molecule, their difference ($\mu(S_1)$ - $\mu(S_0)$), and the transition moment $\mu(S_0 \rightarrow S_1)$, all given in Debye (D). The last column shows the results obtained with the use of B3LYP/STO-3G method, which was also used for the calculations of dipole moments of the whole DBT-DBN system.

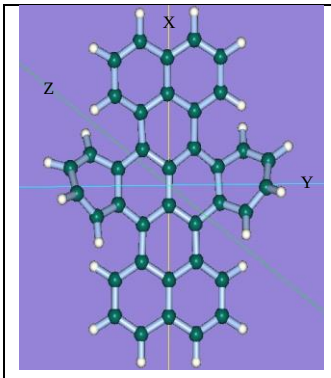

	X	Y	Z	$\|\boldsymbol{\mu}\|$	$\|\boldsymbol{\mu}\|$(STO-3G)
$\mu(S_0)$	-0.626	-0.095	0.287	0.695	0.671
$\mu(S_1)$	-0.168	-0.205	0.265	0.375	0.338
$\mu(S_0 \rightarrow S_1)$	7.770	0.102	-0.282	7.776	8.285
$\mu(S_1)$-$\mu(S_0)$	0.458	-0.110	-0.022	0.472	0.822

Table S2.3: Calculation of the ground state dipole moment of a DBT molecule embedded in a DBN crystal. Components of the dipole moments of (1) an empty cavity created by removing 3 host molecules along the a-axis, (2) the system upon embedding of a DBT molecule into the cavity, and (3) the resulting difference. a, b, c denotes the unit cell axes. Dipole moments are given in Debye [D]. Dipole moments were calculated with the use of TD B3LYP/STO-3G method.

	a	b	c	$\|\boldsymbol{\mu}\|$
(1) Cavity without DBT	-1.750	-0.354	0.232	1.800
(2) DBT in DBN	-1.963	0.724	1.299	2.463
(2) – (1) difference	-0.213	1.079	1.067	1.532

Table S2.4: Quantum chemistry calculations of the electric dipole moments of the ground and excited states of DBT in DBN matrix. Projections of the transition dipole moment μ_{ge} and dipole moments μ_g, μ_e, $\Delta\mu = \mu_e - \mu_g$ of DBT obtained for the different simulation cells. The number of DBN molecules in the simulation cell was varied from 21 to 28.

Calculated system Number of DBN molecules	Dipole moment of empty cavity		*a*-axis	*b*-axis	*c*-axis	$\lvert\boldsymbol{\mu}\rvert$
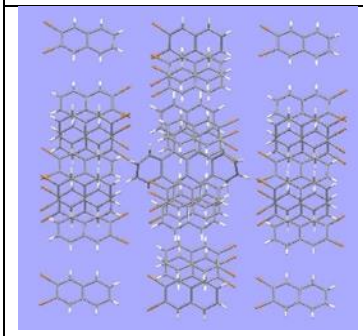 28	6.631	$\mu_{ge}(S_0 \rightarrow S_1)$	8.015	0.382	0.459	8.037
		$\mu_g(S_0)$	-0.615	-0.659	-7.738	7.791
		$\mu_e(S_1)$	0.144	-0.791	-8.420	8.458
		$\mu_e(S_1) - \mu_g(S_0)$	0.759	-0.133	-0.681	1.028
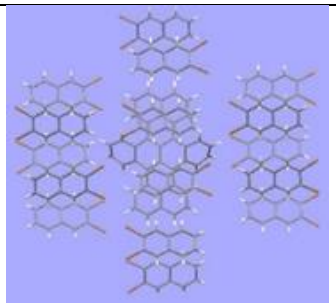 24	0.780	$\mu_{ge}(S_0 \rightarrow S_1)$	7.930	0.434	0.359	7.950
		$\mu_g(S_0)$	-0.276	-0.699	-1.032	1.277
		$\mu_e(S_1)$	0.475	-1.409	-1.165	1.889
		$\mu_e(S_1) - \mu_g(S_0)$	0.751	-0.710	-0.133	1.042
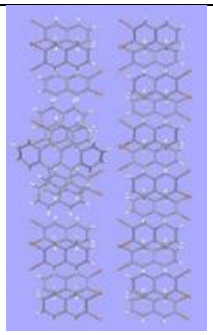 21	1.663	$\mu_{ge}(S_0 \rightarrow S_1)$	-8.513	1.141	-0.104	8.590
		$\mu_g(S_0)$	0.002	-3.634	-0.446	3.661
		$\mu_e(S_1)$	-0.802	-4.214	-0.502	4.319
		$\mu_e(S_1) - \mu_g(S_0)$	-0.804	-0.580	-0.056	0.993

References

(1) B. Lounis, W. E. Moerner, Nature **2000**, 407, 491–493.

(2) Y. L. A. Rezus, S. G. Walt, R. Lettow, A. Renn, G. Zumofen, S. Götzinger, V. Sandoghdar, Phys. Rev. Lett. **2012**, 108, 093601.

(3) G. Wrigge, I. Gerhardt, J. Hwang, G. Zumofen, V. Sandoghdar, Nat. Phys. **2008**, 4, 60–66.

(4) C. Hettich, C. Schmitt, J. Zitzmann, S. Kühn, I. Gerhardt, V. Sandoghdar, Science **2002**, 298, 385–389.

(5) T. Basché, W. E. Moerner, M. Orrit, U. P. Wild, Eds., Single Molecule Optical Detection, Imaging and Spectroscopy, VCH, Weinheim, **1997**.

(6) W. E. Moerner, M. Orrit, Science **1999**, 283, 1670–1676.

(7) Y. Tian, P. Navarro, M. Orrit, Phys. Rev. Lett. **2014**, 113, 135505.

(8) U. P. Wild, F. Güttler, M. Pirotta, A. Renn, Chem. Phys. Lett. **1992**, 193, 451–455.

(9) M. Orrit, J. Bernard, A. Zumbusch, R. I. Personov, Chem. Phys. Lett. **1992**, 196, 595–600.

(10) C. Brunel, P. Tamarat, B. Lounis, J. C. Woehl, M. Orrit, J. Phys. Chem. A **1999**, 103, 2429–2434.

(11) F. Kulzer, R. Matzke, C. Bräuchle, T. Basché, J. Phys. Chem. A **1999**, 103, 2408–2411.

(12) P. Bordat, M. Orrit, R. Brown, A. Würger, Chem. Phys. **2000**, 258, 63–72.

(13) T. Y. Latychevskaia, A. Renn, U. P. Wild, Chem. Phys. **2002**, 282, 109–119.

(14) M. Bauer, L. Kador, J. Lumin. **2002**, 98, 75–79.

(15) M. Bauer, L. Kador, J. Phys. Chem. B **2003**, 107, 14301–14305.(16 P. Bordat, R. Brown, Chem. Phys. Lett. **2000**, 331, 439–445.

(17) T. Plakhotnik, ChemPhysChem **2006**, 7, 1699–1704.

(18) T. Plakhotnik, J. Lumin. **2007**, 127, 235–238.

(19) S. Faez, S. J. van der Molen, M. Orrit, Phys. Rev. B **2014**, 90, 205405.

(20) A. A. L. Nicolet, C. Hofmann, M. A. Kol'chenko, B. Kozankiewicz, M. Orrit, ChemPhysChem **2007**, 8, 1215–1220.

(21) P. Türschmann, N. Rotenberg, J. Renger, I. Harder, O. Lohse, T. Utikal, S. Götzinger, V. Sandoghdar, Nano Lett. **2017**, 17, 4941–4945.

(22) P. Lombardi, A. P. Ovvyan, S. Pazzagli, G. Mazzamuto, G. Kewes, O. Neitzke, N. Gruhler, O. Benson, W. H. P. Pernice, F. S. Cataliotti, C. Toninelli, ACS Photonics **2017**, 5, 126–132

(23) D. Wang, H. Kelkar, D. Martin-Cano, T. Utikal, S. Gçtzinger, V. Sandoghdar, Phys. Rev. X **2017**, 7, 021014.(24) S. Pazzagli, P. Lombardi, D. Martella, M. Colautti, B. Tiribilli, F. S. Cataliotti, C. Toninelli, ACS Nano **2018**, 12, 4295–4303.

(25) C. Kurtsiefer, S. Mayer, P. Zarda, H. Weinfurter, Phys. Rev. Lett. **2000**, 85, 290–293.

(26) X. Ding, Y. He, Z.-C. Duan, N. Gregersen, M.-C. Chen, S. Unsleber, S. Maier, C. Schneider, M. Kamp, S. Höfling, Phys. Rev. Lett. **2016**, 116, 020401.

(27) I. Aharonovich, D. Englund, M. Toth, Nat. Photonics **2016**, 10, 631–641.

(28) A. A. L. Nicolet, P. Bordat, C. Hofmann, M. A. Kol'chenko, B. Kozankie- wicz, R. Brown, M. Orrit, ChemPhysChem **2007**, 8, 1929–1936.

(29) S. Faez, N. R. Verhart, M. Markoulides, F. Buda, A. Gourdon, M. Orrit, Faraday Discuss. **2015**, 184, 251–262.

(30) Y. Tian, P. Navarro, B. Kozankiewicz, M. Orrit, ChemPhysChem **2012**, 13, 3510–3515.

(31) M. Białkowska, W. Chaładaj, A. Makarewicz, B. Kozankiewicz, Acta Phys. Pol. A **2015**, 128, RK.3.1.

(32) M. Białkowska, W. Chaładaj, I. Deperasin´ska, A. Drzewiecka-Antonik, A. E. Koziol, A. Makarewicz, B. Kozankiewicz, RSC Adv. **2017**, 7, 2780–2788.

(33) Gaussian 09, Revision B.01, M. J. Frisch, G. W. Trucks, H. B. Schlegel, G. E. Scuseria, M. A. Robb, J. R. Cheeseman, G. Scalmani, V. Barone, B. Mennucci, G. A. Petersson, H. Nakatsuji, M. Caricato, X. Li, H. P.Hratchian, A. F. Izmaylov,, J. Bloino, G. Zheng, J. L. Sonnenberg, M. Hada, M. Ehara, K. Toyota, R. Fukuda, J. Hasegawa, M. Ishida, T. Nakajima, Y. Honda, O. Kitao, H. Nakai, T. Vreven, Jr. J. A. Montgomery, J. E. Peralta, F. Ogliaro, M. Bearpark, J. J. Heyd, E. Brothers, K. N. Kudin, V. N. Staroverov, T. Keith, R. Kobayashi, J. Normand, K. Raghavachari, A. Rendell, J. C. Burant, S. S. Iyengar, J. Tomasi, M. Cossi, N. Rega, J. M. Millam, M. Klene, J. E. Knox, J. B. Cross, V. Bakken, C. Adamo, J. Jaramillo, R. Gomperts, R. E. Stratmann, O. Yazyev, A. J. Austin, R. Cammi, C. Pomelli, J. W. Ochterski, R. L. Martin, K. Morokuma, V. G. Zakrzewski, G. A. Voth, P. Salvador, J. J. Dannenberg, S. Dapprich, A. D. Daniels, O. Farkas, J. B. Foresman, J. V. Ortiz, J. Cioslowski, D. J. Fox, Gaussian Inc., Wallingford CT, **2010**

(34) I. Deperasin´ska, B. Kozankiewicz, Chem. Phys. Lett. **2017**, 684, 208–211.

(35) C. R. Groom, I. J. Bruno, M. P. Lightfoot, S. C. Ward, Acta Crystallogr. Sect. B Struct. Sci. Cryst. Eng. Mater. **2016**, 72, 171–179.

(36) P. T rschmann, N. Rotenberg, J. Renger, I. Harder, O. Lohse, T. Utikal, S. Götzinger, V. Sandoghdar, ArXiv:1702.05923v1 Cond-Mat Physics **2017**.

(37) I. Deperasin´ska, E. Karpiuk, M. Banasiewicz, B. Kozankiewicz, Chem. Phys. Lett. **2010**, 492, 93–97